J Mater Sci (2024) 59:1433–1447

Computation & theory

Designing Pr-based advanced photoluminescent materials using machine learning and density functional theory

Upendra Kumar[1], Hyeon Woo Kim[1,2], Sobhit Singh[3], Sung Beom Cho[4,*], and Hyunseok Ko[1,*]

[1] *Carbon Neutrality and Digitalization Division, Korea Institute of Ceramic Engineering and Technology (KICET), Jinju 52851, South Korea*
[2] *Department of Materials Science and Engineering, Hanyang University, Seoul 04763, South Korea*
[3] *Department of Mechanical Engineering at the University of Rochester, New York 14611, United States*
[4] *Department of Energy Systems Research, Ajou University, Suwon 16499, South Korea*

Received: 19 June 2023
Accepted: 2 December 2023
Published online: 11 January 2024

© The Author(s), under exclusive licence to Springer Science+Business Media, LLC, part of Springer Nature, 2024

ABSTRACT

This work presents a machine learning approach to predict novel perovskite oxide materials in the Pr-Al-O and Pr-Sc-O compound families with the potential for photoluminescence applications. The predicted materials exhibit a large bandgap and high Debye temperature, and have remained unexplored thus far. The predicted compounds (Pr_3AlO_6, $Pr_4Al_2O_9$, Pr_3ScO_6 and $Pr_3Sc_5O_{12}$) are screened using machine learning approach, which are then confirmed by density functional theory calculations. The study includes the calculation of the bandgap and density of states to determine electronic properties, and the optical absorption and emission spectra to determine optical properties. Mechanical stability of the predicted compounds, as demonstrated by satisfying the Born-Huang criterion. By combining machine learning and density functional theory, this work offers a more efficient and comprehensive approach to materials discovery and design.

Handling Editor: Ghanshyam Pilania

Upendra Kumar and Hyeon Woo Kim have contributed equally to this work and should be considered co-first authors.

Address correspondence to E-mail: csb@ajou.ac.kr; hko@kicet.re.kr

https://doi.org/10.1007/s10853-023-09232-6

GRAPHICAL ABSTRACT

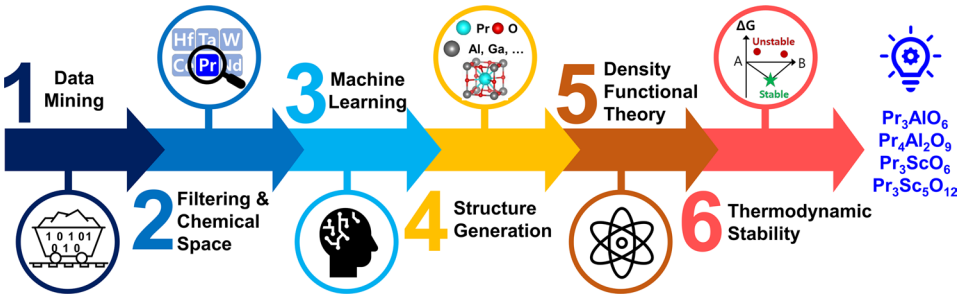

Introduction

In recent years, notably, two distinct subclasses of perovskites, i.e., halide perovskites and oxide perovskites have concurrently gained significant prominence within the photovoltaics research landscape [1]. Luminescent materials based on perovskite halides, exemplified by methylammonium lead iodide ($MAPbI_3$), have demonstrated significant potential in photovoltaic and optoelectronic applications [2]. However, the stability of these materials presents a substantial challenge, particularly due to their susceptibility to moisture and oxygen under ambient conditions [3]. Conversely, there has been a recent resurgence of interest in the perovskites oxide for photovoltaic applications. This resurgence is attributed to their fundamentally new photovoltaic mechanisms, capable of generating a photovoltage well beyond the bandgap, potentially leading to enhanced energy conversion efficiency. Therefore, it is needed to explore and discover of new perovskite oxides materials, which have remained relatively under-explored.

Furthermore, a majority of perovskite oxides exhibit rigid stability on humidity, however, they are not considered as common photovoltaic materials due to their wide band-gap energies. Nonetheless, some of perovskite oxides shows excellent and distinct optical properties. These properties are utilized in the development of advanced optoelectronic devices, such as nonlinear optics crystals [4, 5], scintillators [6], photoluminescent (PL) and electroluminescent materials [7, 8], as well as solar cells [9]. Novel PL bands have been observed in $SrTiO_3$, which is a typical example of a perovskite semiconductor [10, 11]. Perovskite oxide derivatives offer an attractive alternative to perovskite halides for luminescent applications [12]. These materials are often more thermally stable [13] and less toxic [14] than their halide counterparts, and can exhibit desirable electronic and optical properties. Furthermore, perovskite oxide derivatives provide a diverse design space that allows for the incorporation of traditional luminescent elements such as Cr, Yb, Pr, Eu, Tb, and others. The chemical space of perovskite oxide derivatives is not fully explored yet, offering a promising avenue for the development of new luminescent materials.

Perovskite oxides are promising scintillators due to their high light yield and fast response time [15]. They emit more photons per unit of absorbed radiation than other materials, making them useful for detecting high-energy particles and reducing the risk of radiation damage to sensitive equipment [16]. Additionally, perovskite oxide scintillators have the potential to overcome the stability issues of perovskite halide scintillators. While perovskite halide scintillators have high light yield and fast response times, they are known to be unstable under certain conditions such as exposure to moisture and high temperatures. Several types of perovskite oxide scintillators have been studied, including strontium titanate ($SrTiO_3$) [17], barium titanate ($BaTiO_3$) [18], and lanthanum aluminate ($LaAlO_3$) [19], which have shown promising results in terms of their light yield and response time. Therefore, ongoing research is focused on improving their performance and understanding their underlying physics.

The motivation for studying Praseodymium (Pr)-based photovoltaic materials stems from the desire to explore lead-free alternatives and diversify material options in the field of photovoltaics. While there is a need to delve into the synthesizability of Pr-based compounds, expanding the range of materials used in photovoltaics is essential for finding more efficient, cost-effective, and versatile solutions. Investigating

Pr-based perovskites diversifies the material portfolio for solar cells, potentially leading to enhanced performance, stability, and compatibility with various applications. Exploring Praseodymium (Pr)-based perovskites in photovoltaics is driven by their potential to address critical challenges such as stability, toxicity, and material availability. Shun et al. [20] conducted a study on Pr-doped triple-cation perovskite layers, revealing that 0.25% Pr doping significantly improves the efficiency and stability of perovskite solar cells. This enhancement results from improved carrier mobility, reduced carrier recombination, and lattice shrinkage, offering a novel approach for high-performance perovskite solar cells. In a separate study, Vert et al. [21] developed active perovskite-based solid oxide fuel cell cathodes by combining lanthanides (La, Pr, Sm) in the $Ln_{0.58}Sr_{0.4}Fe_{0.8}Co_{0.2}O_{3-\delta}$ system. This approach improved electrochemical properties, reducing electrode polarization resistance and enhancing performance. The most effective composition was identified as a praseodymium-rich lanthanum-based electrode material. Nonlinear functions were employed to model experimental data, enabling the identification of an electrode composition that minimized polarization resistance while maintaining reduced activation energy. Electrochemical characterization further supported the cooperative effect of lanthanide combinations. Praseodymium-based perovskites unique properties and tunability make them attractive candidates for future solar energy technologies. Despite potential challenges in synthesis and optimization, their benefits could lead to innovative and sustainable advancements in photovoltaics and beyond.

By conducting data mining from the Materials Project [22], we have identified that Pr-Al-O and Pr-Sc-O materials have been relatively underexplored to date. These materials exhibit high Debye temperatures and larger bandgaps, as visually represented in Fig. 1 of supplementary. In this study, we have identified under-explored Pr-based perovskite oxides and predicted new promising compounds for photovoltaic applications. By combining machine learning and data mining, we found that Pr-based perovskites are relatively under-explored compared to other types. The focus of this work is on predicting perovskite oxide materials in the Pr-Al-O and Pr-Sc-O families, known for their larger bandgap and Debye temperature, as potential candidates for photoluminescence applications. Machine learning is employed to screen a vast number of materials and predict their electronic and optical properties. To validate the predictions, density functional theory (DFT) calculations are performed to study the band structure, density of states, optical absorption, emission spectra, as well as elastic and mechanical stability. This integrated approach of machine learning and DFT offers a more efficient and comprehensive method for materials discovery and design, facilitating the identification of perovskite oxide materials with desirable electronic and optical properties for photoluminescence applications.

Methods

Dataset and features

We have successfully retrieved a comprehensive dataset from the Materials Project [22]. This dataset encompasses various essential physical quantities, including material identification, pretty formula representation, bandgap values, convex hull information, space-group symbols, ICSD (Inorganic Crystal Structure Database) identifiers, structural details, elasticity characteristics, CIF (Crystallographic Information File) data, and Debye temperature values. In total, this dataset is comprised of 1346 rows and 10 columns, making it a valuable resource for conducting diverse research and analyses within the field of materials science. The features within the CGCNN model originate from the crystal graph (crystallographic information files), effectively encapsulating the structural details of the crystal system.

ML technique

The innovative generalized Crystal Graph Convolutional Neural Networks (CGCNN) framework, introduced by T. Xie and J. C. Grossman [23], is tailored for representing periodic crystal systems, offering a dual advantage of accurately predicting material properties in alignment with density functional theory and providing atomic-level chemical insights. Inspired by recent advancements in deep learning, akin to learning from raw data representations, the authors [23] extend this concept to crystal structures. CGCNN leverages convolutional neural networks built upon crystal graphs derived from these structures, demonstrating exceptional accuracy akin to DFT calculations across eight distinct material properties when trained on

Materials Project data. Notably, CGCNN's interpretability is showcased by extracting site-specific energy contributions within perovskite structures, elucidating the influence of local chemical environments on global properties. By encapsulating atomic information and bonding interactions within crystal graphs, this method enables neural networks to autonomously derive optimal representations for property prediction, streamlining the search for stable perovskite materials and enhancing high-throughput screening efforts. Essentially, this innovation bridges the theory-experiment gap in materials science by fusing crystal graphs and convolutional neural networks. Approximately 70% of the data, which equates to around 942 samples, is designated for training purposes, while another 15% (approximately 202 samples) is set aside for testing, and an additional 15% (also around 202 samples) is allocated for validation. The number of total epochs is 30 CGCNN model.

Performance curve

The performance curve of the ML model is depicted in Fig. 1. R^2, a statistical measure of the proportion of variance explained by the model, reaching its maximum signifies that the model effectively captures the variability in the dependent variable. This implies a strong correlation between the predicted and observed values. Simultaneously, achieving the minimum root mean square error (RMSE), which quantifies the average magnitude of the model's errors, across all datasets reflects the high precision and accuracy of the model's predictions. Consistency in optimizing both R^2 and minimizing RMSE across training, testing, and validation datasets affirms the model's generalizability, indicating its capacity to perform well not only on the data it was trained on but also on new, unseen data, thereby establishing its reliability and predictive power. The assertion that the R^2 value is maximized and the RMSE is minimized across training for 70% datasets proves the robust performance of the predictive model.

DFT method

The Vienna ab initio simulation package (VASP), which uses the projector augmented wave method (PAW), is used to perform all the reported DFT calculations in this work [24, 25]. Exchange and correlation energies are computed using the generalized gradient approximation provided as parameterized by Perdew-Burke-Ernzerhof (PBE) [26]. Brillouin zone is constructed using a Γ-centered (3×3 ×5 for Pr_3AlO_6 and 2×3 ×2 for $Pr_4Al_2O_9$) and Monkhorst-Pack (4×4×4 for Pr_3ScO_6 and 2×2 ×2 for $Pr_3Sc_5O_{12}$) type k-meshes [27]. In all DFT calculations, we employed a plane wave cut-off energy of 400 eV. We used 10^{-4} eV/Å as the force convergence criterion to relax the inner-atomic coordinates, and 10^{-6} eV as the energy convergence criterion for self-consistence DFT calculations. In the quest for discovering new photoluminescent materials, a comprehensive and systematic approach has been employed, as illustrated in the devised flow chart. The process initiates with data mining

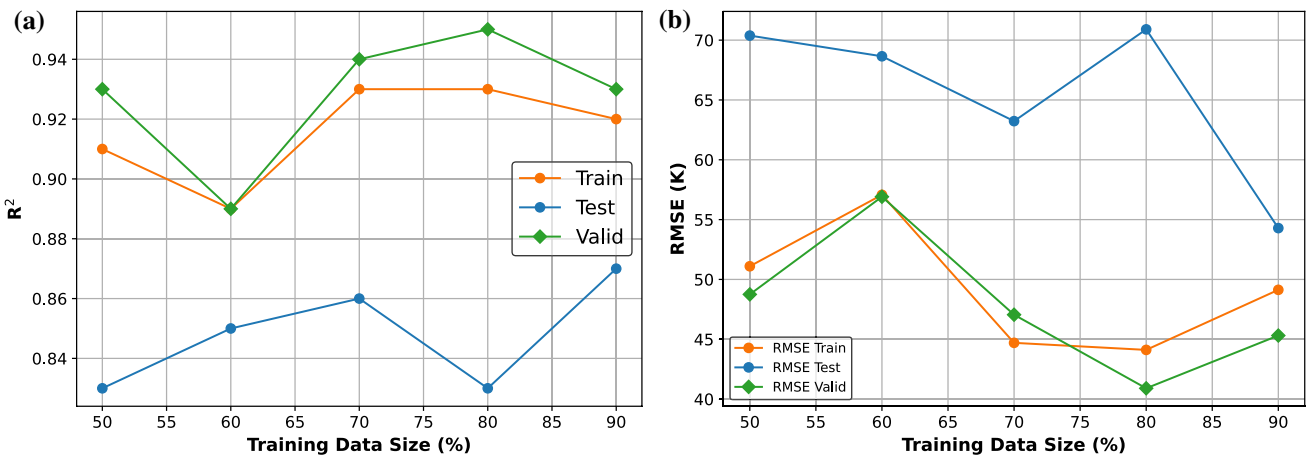

Figure 1 (**a**) The plot between training data and R^2 and (**b**) Training data and root mean square error (RMSE), i.e., learning curve. The testing and validation data are complementary to training data.

(1), wherein extensive databases are scrutinized to extract pertinent information about known materials and their photoluminescent properties. Subsequently, the filtration and exploration of chemical space (2) are undertaken, aiming to identify potential candidates based on specific criteria. The integration of machine learning techniques (3) enhances the predictive capabilities by extrapolating patterns from the amassed data. Following this, the generation of crystal structures (4) is executed to propose novel material configurations. The application of density functional theory (5) is pivotal in assessing the electronic and optical properties of these structures, ensuring their viability for photoluminescence. Finally, thermodynamic stability analysis (6) is employed to validate the feasibility of the proposed materials, offering a holistic and rigorous approach to predicting new photoluminescent materials with enhanced accuracy and efficiency. The comprehensive workflow can be grasped by referring to the schematic diagram provided in Fig. 2.

Results and discussion

The Debye temperature (Θ_D) is the maximum temperature that can be attained as a result of a single normal-mode vibration, i.e., the temperature of a crystal's highest normal mode of vibration. It is a good indicator of structural stiffness, which makes it suitable for evaluating photoluminescent quantum yield [28]. However, there are a number of limitations to utilizing the DFT method to compute Θ_D, i.e., doing so is computationally expensive. Instead, it is also possible to predict Θ_D for many compounds using machine learning [29], which is computationally less expensive than DFT. Still, knowing only the Θ_D of a crystal structure is insufficient to achieve a high photoluminescence quantum efficiency: *a wide bandgap is also required*. Plotting Θ_D as a function of DFT determined bandgap, which serves as a sorting diagram, allows for the final optimization of these two features. There is a dependency of Θ_D on the energy band gap (E_g) in the semiconducting material [30]. Therefore, it is necessary to find the value of bandgap and Θ_D for a good photoluminescence material.

Advanced ML-based methods have revolutionized the field of material science by providing an alternative to traditional experimental trial-and-error and computationally expensive DFT calculation techniques [31]. In the Pearson's crystal database (PCD) [32], the machine learning has been used to predict Θ_D for a majority of compounds. Therefore, we performed data mining for O, Se, S and Te-based chalcogen ternary compounds by using materials project [22] database, as shown in Fig. 3a. It is found that oxide-based materials consist large bandgap and high Debye temperature among the studied chalcogen family. Since data availability for Debye temperature is very limited in the materials-project database [22], we employed CGCNN [23] for calculating Debye temperature with the crystallographic information files as an input feature. The CGCNN is able to predict the Debye temperature with accuracy of 93% as shown in Fig. 3b.

We started our data mining process using the materials-project database [22] to explore the relatively under-explored perovskite oxide family containing Cr, Eu, Yb, and Pr elements, as shown in Fig. 4, with further details provided in

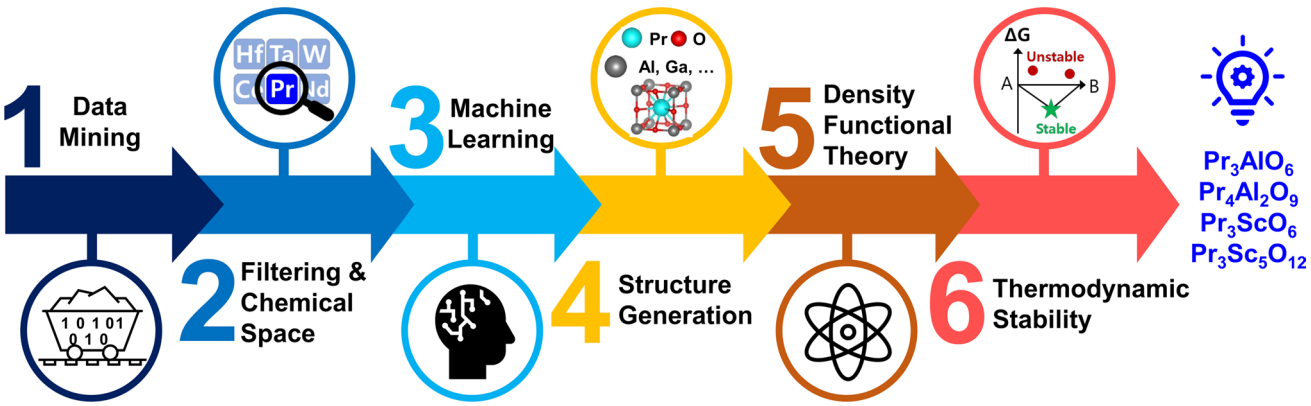

Figure 2 Schematic flowchart of the proposal to discover new materials.

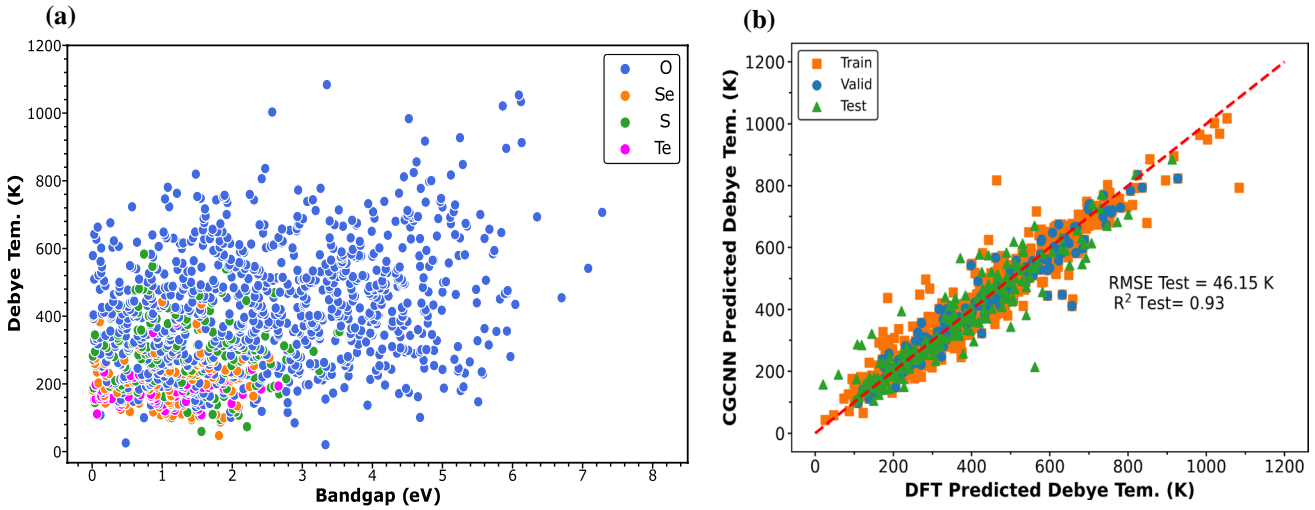

Figure 3 (**a**) Plot between Debye temperature and bandgap of chalcogenide perovskites family. (**b**) Plot between DFT (PBE) predicted vs CGCNN predicted values of Debye temperature.

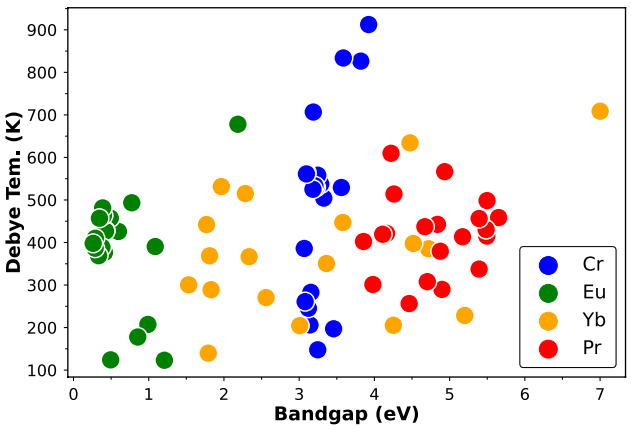

Figure 4 Plot between Debye temperature and bandgap of Cr-based, Eu-based, Yb-based, and Pr-based ternary perovskites oxide family.

supplementary section (I). After screening several promising photoluminescent materials using data mining, we found that Praseodymium (Pr) is the least explored element in this family. Therefore, we focused on the ternary compounds of the Pr-based perovskite oxide family, which have a large bandgap and high Debye temperature, as depicted in Fig. 4. Among the Pr-based perovskite oxide family, the Pr-Sc-O and Pr-Al-O subfamilies are the least explored. We found only two well-known materials having zero energy above the convex hull (E_{hull}) in the materials-project database [22], as described in supplementary section (I:D) [22]. Hence, we explored these families to predict new candidate structures for potential photoluminescence applications.

Hautier et al. [33] introduced a novel probabilistic model designed to evaluate the feasibility of ionic species substituting for one another while preserving the crystal structure. This pioneering model leverages an extensive experimental database of crystal structures for its training. Inspired by techniques from the field of machine translation, this model incorporates substitution knowledge into a specialized probability function. This function can be employed to quantitatively gauge the probability that a particular substitution will result in the formation of another stable compound maintaining the same crystal structure. Recently, H. Kim et al. [34] adopted a same approach, as described by Hautier et al. [33], to predict the emergence of a novel halide perovskite, specifically Cs_3LuCl_6. This underscores the continued utility and effectiveness of the model in predicting new compounds with desired crystal structures in the realm of materials science. We provide the code used for the structure predictor, given in supplementary section(II). In this work, we utilize the same machine learning model for the prediction of new structures in Pr-Al-O and Pr-Sc-O ternary compound families. In the case of Pr-Al-O family, there are only three obtained compositions, i.e., **(i)** $Pr_4Al_2O_9$ **(ii)** $PrAlO_3$ and **(iii)** Pr_3AlO_6 having zero energy above the convex hull. We note, $PrAlO_3$ has already been in the category

of well-known compound [22]. Therefore, there are only two remaining candidates, i.e., **(i)** $Pr_4Al_2O_9$ and **(ii)** Pr_3AlO_6, which can be considered as novel candidates in this work. Similarly, in the case of Pr-Sc-O family, the compounds Pr_3ScO_6 and $Pr_3Sc_5O_{12}$ are considered as novel candidates in this work. All the details of newly predicted compounds are given in Table 1. Their structures are shown in Fig. 5.

Getting the formation energy and building the related convex hull is a crucial step in figuring out if a compound is energetically stable [35]. From thermodynamical point of view, the convex hull belongs to the Gibbs free energy of the compounds at zero temperature. Our calculations reveal that the newly predicted compounds are energetically stable, as confirmed by the convex hull plot shown in Fig. 6. Further details, including E_{hull} and parent atom details, are provided in supplementary section (III).

Bandgap and density of states

We calculated electronic bandgap of the newly predicted compounds using PBE-DFT [26], CGCNN, and modified Becke Johnson (mBJ) [36] methods. For further improving the accuracy of the bandgap, we utilized computationally more expensive hybrid functional – Heyd-Scuseria-Ernzerhof (HSE06) [37]. All the calculated bandgap values are reported in Table 2. We have also calculated Debye temperature of the newly predicted compounds using CGCNN [23] and validated it with DFT calculations, as mentioned in Table 2. All the predicted compounds have a large bandgap and high Debye temperature. Direct band gap semiconductors allow for efficient production of photons without assistance from phonons due to the aligned valence and conduction band extrema. This makes them highly desirable for optical devices, i.e., for photoluminescence applications. So, the newly predicted compounds $Pr_4Al_2O_9$ and $Pr_3Sc_5O_{12}$ are better suited for photoluminescence applications, as shown in Fig. 7.

DOS plays a crucial role in defining the characteristics of the materials [38]. In order to learn more about the electronic structure of the predicted compound, we have calculated the total and atomic-orbitals resolved electronic DOS, as shown in Fig. 7, respectively. In predicted compounds major contribution is because of *p* orbital of oxygen and *d* orbital of Pr and Sc. In DOS of Pr_3AlO_6, shown in Fig. 7a, the peak around −4.3 eV is due to the hybridization of all elements. In case of valance band maximum major contribution in the total DOS is due to *p* orbital of oxygen. But in case of conduction band minimum, the *d* orbital of Pr has a major contribution to the total DOS. The *s* orbital of Al is also playing a role in making larger peak around −4.3 eV. Similar behavior can be also seen for the $Pr_4Al_2O_9$, depicted in Fig. 7b. But, here, *s* orbital of Al contribution can be seen around -4 eV. So, electronic transitions from O–*p* orbitals to Pr–*d* orbitals are possible. Similar pattern of DOS can be seen for the Pr_3ScO_6 and $Pr_3Sc_5O_{12}$ compound, depicted in Fig. 7c, d.

Table 1 The structural details of newly predicted compounds

	Lattice parameters (Å)	Lattice angle	Space group type	Crystal structure	Space group number
Pr_3AlO_6	a = 7.47 b = 7.47 c = 5.62	$\alpha = 90°$ $\beta = 90°$ $\gamma = 102.80°$	$Cmc2_1$	Orthorhombic	36
$Pr_4Al_2O_9$	a = 11.02 b = 7.85 c = 11.50	$\alpha = 70.54°$ $\beta = 90°$ $\gamma = 90°$	$P2_1/c$	Monoclinic	14
Pr_3ScO_6	a = 6.89 b = 6.89 c = 6.89	$\alpha = 92.38°$ $\beta = 92.38°$ $\gamma = 92.38°$	$R\bar{3}$	Trigonal (Rhombohedral)	148
$Pr_3Sc_5O_{12}$	a =11.39 b = 11.39 c = 11.39	$\alpha = 109.47°$ $\beta = 109.47°$ $\gamma = 109.47°$	$Ia\bar{3}d$	Cubic	230

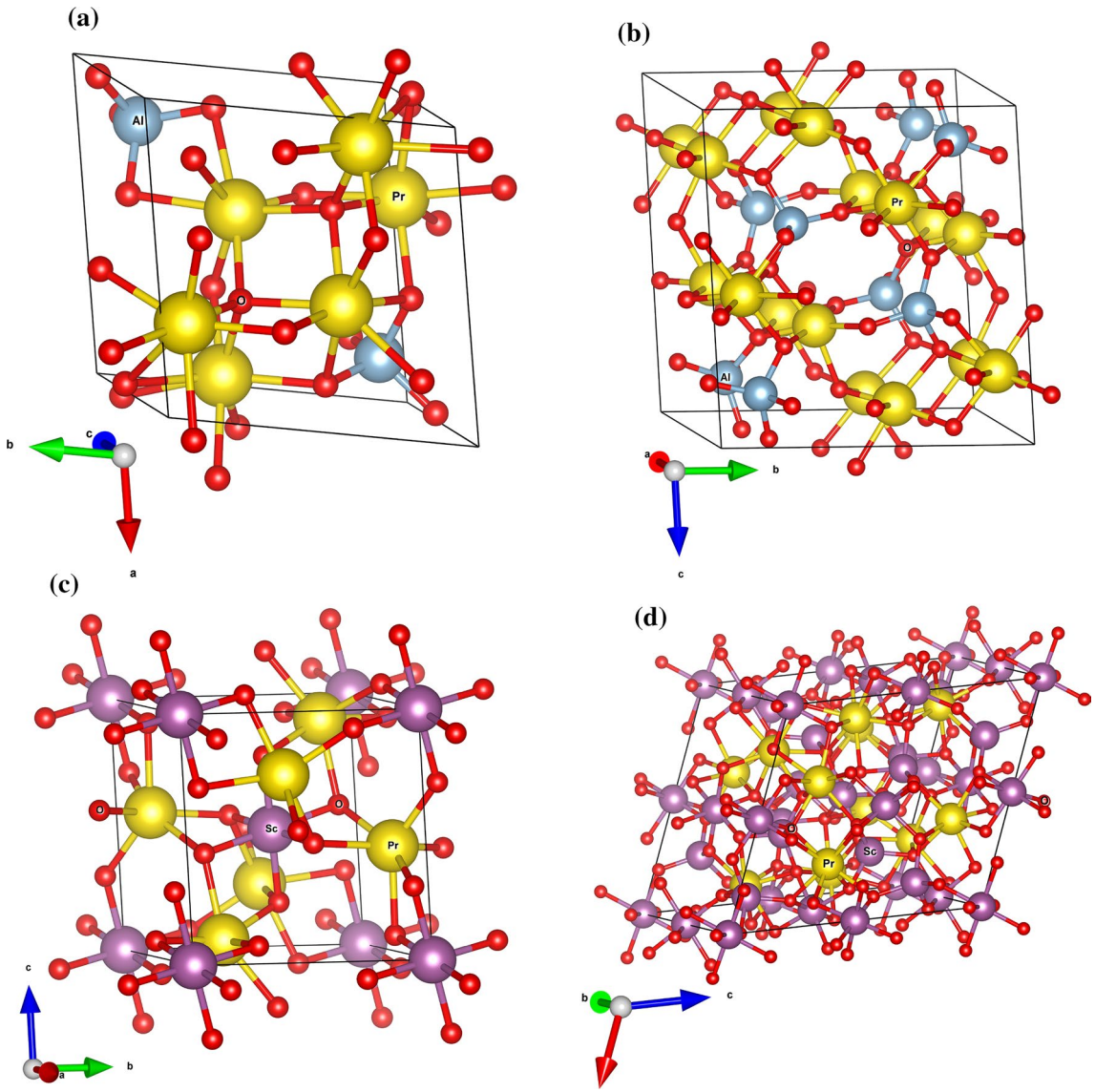

Figure 5 Crystal structures of (**a**) Pr_3AlO_6 ($Cmc2_1$), (**b**) $Pr_4Al_2O_9$ ($P2_1/c$), (**c**) Pr_3ScO_6 ($R\bar{3}$), and (**d**) $Pr_3Sc_5O_{12}$ ($Ia\bar{3}d$).

Optical spectra

It is possible to derive the linear optical properties from the frequency-dependent complex dielectric function $\varepsilon(\omega)$:

$$\varepsilon(\omega) = \varepsilon_1(\omega) + i\varepsilon_2(\omega). \tag{1}$$

where the real and imaginary components of the dielectric function are denoted by $\varepsilon_1(\omega)$ and $\varepsilon_2(\omega)$, respectively, ω represents the frequency of the photon. The real components $\varepsilon_1(\omega)$ can be obtained by using the Kramers-Krönig relationship [39] and imaginary components $\varepsilon_2(\omega)$ can be calculated by using momentum matrix elements between the valence and conduction wave functions [40, 41]. With the help of $\varepsilon_1(\omega)$ and $\varepsilon_2(\omega)$, the refractive index $n(\omega)$ and absorption coefficient $\alpha(\omega)$ can be calculated by using formula:

$$n(\omega) = \left[\frac{\sqrt{\varepsilon_1^2 + \varepsilon_2^2} + \varepsilon_1}{2}\right]^{\frac{1}{2}}, \text{ and} \tag{2}$$

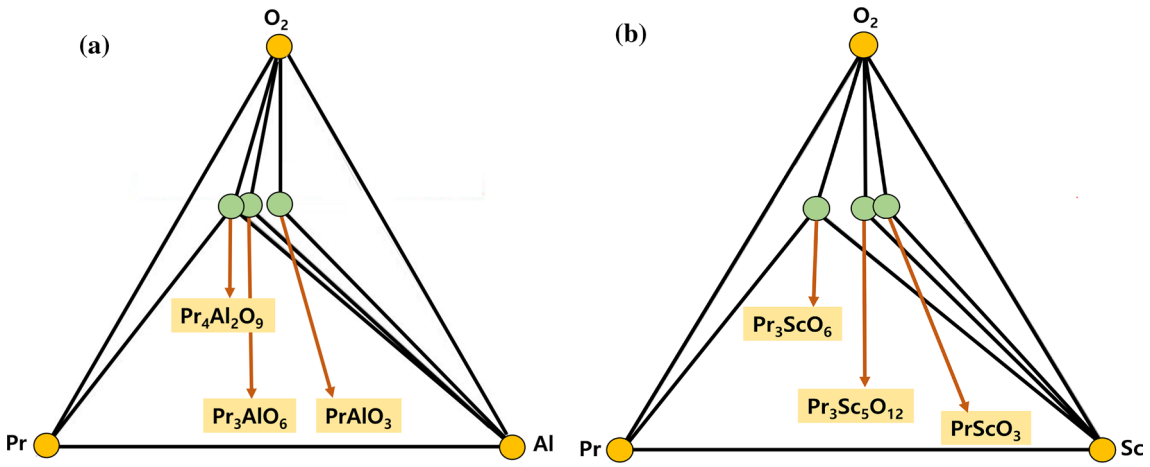

Figure 6 The convex hull plot of (**a**) Pr-Al-O (**b**) Pr-Sc-O family. The $PrAlO_3$ and $PrScO_3$ represent known compounds of the materials-project database [22], and others are newly predicted compounds by our ML combined with DFT method.

Table 2 Bandgap and Debye temperature of newly predicted compounds. The DFT-PBE data are used for training the CGCNN model

	Bandgap DFT-PBE (eV)	Bandgap CGCNN (eV)	Bandgap DFT-mBJ (eV)	Bandgap DFT-HSE (eV)	Debye Temp. CGCNN (K)	Debye Temp. DFT-PBE (K)	Bandgap type
Pr_3AlO_6	4.18	4.18	5.69	5.67	393.98	398.78	Indirect
$Pr_4Al_2O_9$	4.07	3.84	6.07	5.56	428.87	431.33	Direct
Pr_3ScO_6	4.29	4.15	5.46	5.80	410.60	390.24	Indirect
$Pr_3Sc_5O_{12}$	3.83	3.44	5.12	5.32	488.55	486.34	Direct

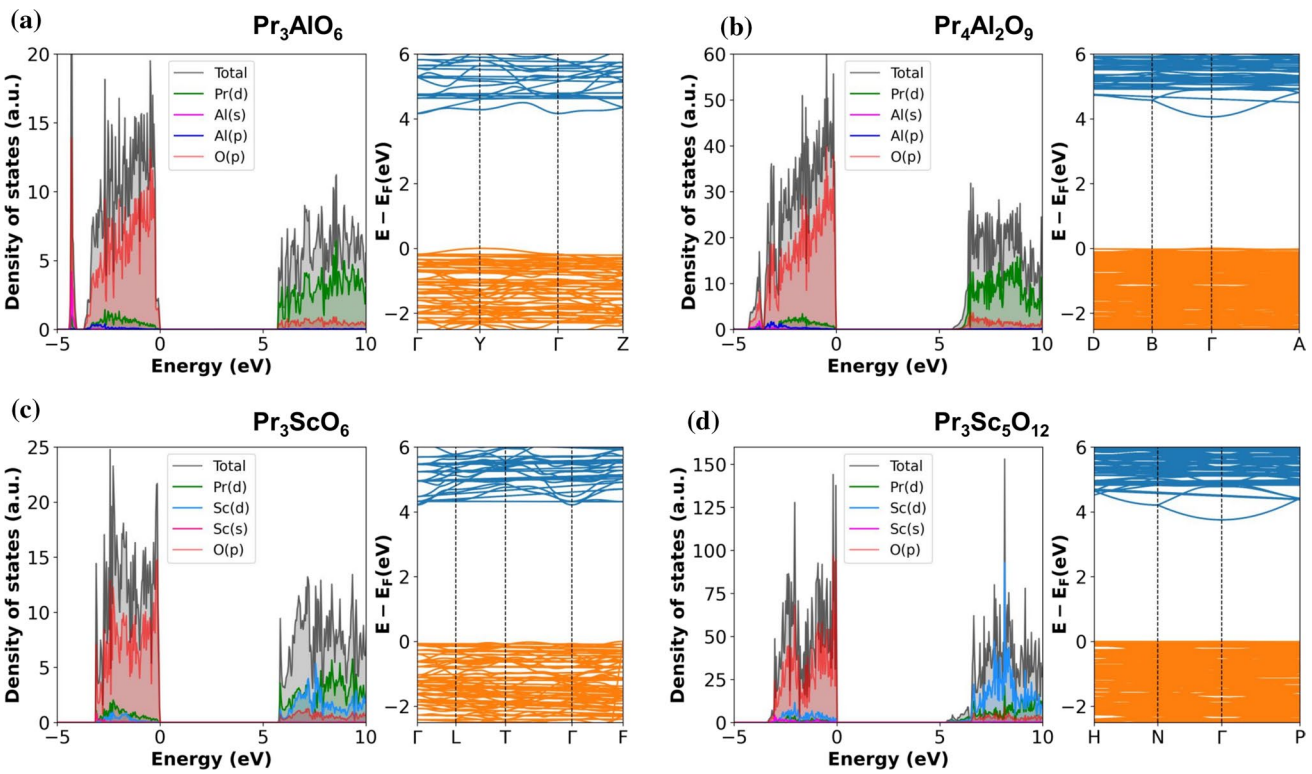

Figure 7 Total HSE06 electronic density of states and PBE-calculated electronic band structure of newly predicted compounds.

$$\alpha(\omega) = \sqrt{2}\omega\left[\frac{\sqrt{\varepsilon_1^2+\varepsilon_2^2}-\varepsilon_1}{2}\right]^{\frac{1}{2}}. \quad (3)$$

For predicted anticipated compounds, the computed $\varepsilon_1(\omega)$ and $\varepsilon_2(\omega)$ as a function of ω are shown in Fig. 8. The maximum peak of real part can be seen at 6.73 eV ($\varepsilon_1(\omega) = 3.17$) for Pr_3AlO_6, 6.84 ($\varepsilon_1(\omega) = 2.84$) eV for $Pr_4Al_2O_9$, 6.81 eV ($\varepsilon_1(\omega) = 3.43$) for Pr_3ScO_6 and 7.13 eV ($\varepsilon_1(\omega) = 3.51$) for $Pr_3Sc_5O_{12}$ compounds. The zero frequency limits ($\omega \to 0$) of $\varepsilon_1(\omega)$ could be used to calculate the static dielectric constants. Static dielectric constants are determined to be 1.75 for Pr_3AlO_6, 1.60 for $Pr_4Al_2O_9$, 3.43 for Pr_3ScO_6, and 1.69 for $Pr_3Sc_5O_{12}$. The $\varepsilon_2(\omega)$ in Fig. 8b shows that the dielectric function's threshold energy is at about 5.1 eV. This is equivalent to the fundamental absorption edge, which is the optical transition between the valence band maximum (VBM) and the conduction band minimum (CBM). The absorptive portion of $\varepsilon_2(\omega)$ displays two dominating peaks at nearly 10 eV and 25 eV as the energy increases. The first peak is caused by O−2p electrons transitioning into the s states of cations, but the subsequent peak may correspond to O−2p electrons transitioning into the p states of cations [42].

The decay of light intensity propagating over a unit distance in a material is described by the absorption coefficient $\alpha(\omega)$. According to Fig. 9a, the absorption edge begins to appear at around 5 eV. This is caused by excited electrons transitioning from O−2p states at the top of the valence band to empty cation 2s states. Take note that, the $\alpha(\omega)$ is seen at a value lower than 5 eV, i.e., ultraviolet range. On the other hand, these compounds display a noticeable absorption due to the fact that the absorption coefficient rapidly increases when the photon energy is greater than the absorption edge. This is a property that is typical of semiconductors and insulators. In Fig. 9b, the measured curve of $n(\omega)$ as a function of photon energy is shown. It should be noted that the static refractive index $n(0)$ values for incoming light are 0.94 for Pr_3AlO_6, 0.89 for $Pr_4Al_2O_9$, 0.95 for Pr_3ScO_6 and 0.92 for $Pr_3Sc_5O_{12}$ compounds. At a photon energy around 7 eV, the refractive index $n(\omega)$ achieves its maximum value. After that, the energy level gradually decreases until it reaches its lowest point, after which it hardly changes at all in the high energy zone (≥50 eV).

Mechanical property

To ensure that a material is properly included into the developing technology, it is essential to extensively analyze its mechanical characteristics. By applying the Born criterion, we assess the mechanical stability [43]. The elastic tensor matrix is obtained using finite lattice distortions and the strain–stress relationship. In order to account for the relaxation of rigid ions, the elastic tensor matrix (C_{ij}) has been computed. The coefficients are measured in gigapascals (GPa). The `MechElastic Python module` [44] is used for the

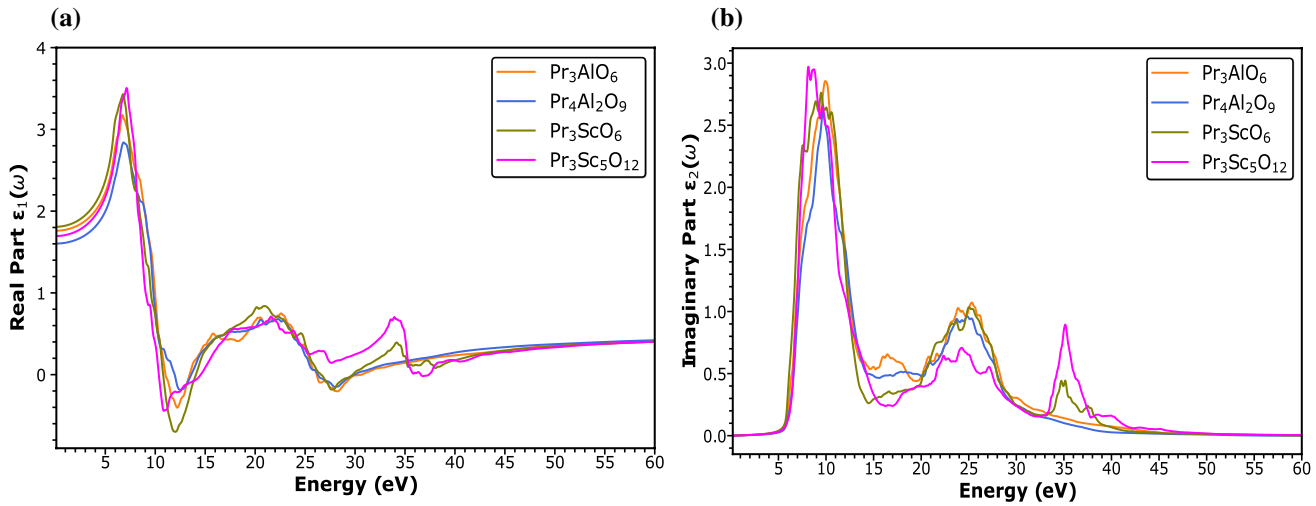

Figure 8 HSE06 calculated (**a**) real part $\varepsilon_1(\omega)$ and (**b**) imaginary part $\varepsilon_2(\omega)$ of the complex dielectric function.

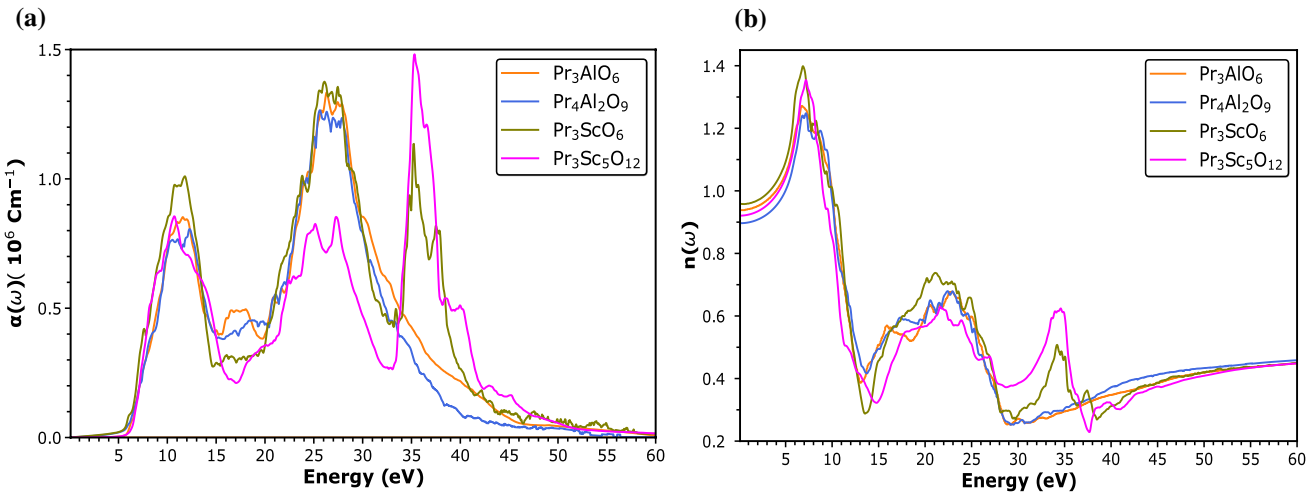

Figure 9 HSE06 calculated (**a**) absorption $\alpha(\omega)$ and (**b**) refractive $n(\omega)$ spectrum.

Table 3 Calculated material properties of predicted structures

Parameters	Pr_3AlO_6	$Pr_4Al_2O_9$	Pr_3ScO_6	$Pr_3Sc_5O_{12}$
Bulk modulus (GPa)	121.19	117.97	128.86	128.84
Shear modulus (GPa)	52.37	56.60	50.45	61.48
Young's modulus (GPa)	137.33	146.39	133.86	159.14
Poisson's ratio	0.31	0.29	0.33	0.29

mechanical characteristics of newly predicted compounds by utilizing the elastic coefficient matrix (C_{ij}) generated from any ab-initio density-functional theory (DFT) method. The elastic tensor matrices are given in the Appendix. All of the Born criterion are met by the coefficient produced using DFT-PBE, indicating that all predicted structures are mechanically stable. Other mechanical properties-related parameters are listed in Table 3.

Poisson's ratio values for the given compounds contribute to the assessment of their ductility and strength. The relation between Poisson's ratio (ν), Young's modulus (E) and shear modulus (G) is:

$$\nu = \frac{E}{2G} - 1. \tag{4}$$

The provided Poisson's ratio values for the materials offer insights into their ductility and strength. Higher Poisson's ratios, as observed in Pr_3AlO_6 (0.31) and Pr_3ScO_6 (0.33), suggest a greater tendency to deform laterally under stress, indicative of potential ductility. On the other hand, lower Poisson's ratios, seen in $Pr_4Al_2O_9$ (0.29) and $Pr_3Sc_5O_{12}$(0.29), imply less lateral deformation and potentially higher stiffness, which may be associated with increased strength.

Comparing the Poisson's ratio values of the predicted materials (Pr_3AlO_6, $Pr_4Al_2O_9$, Pr_3ScO_6, and Pr3 Sc5O12) with those of well-known ferroelectric ceramics like $PbTiO_3$ and $SnTiO_3$ reveals distinct mechanical behaviors. The Poisson's ratio values for $PbTiO_3$ are 0.26 [45], and for $SnTiO_3$ are 0.28 [45], typically low, as these materials are known for their high stiffness and resistance to lateral deformation. In contrast, the higher Poisson's ratios observed in the predicted materials (ranging from 0.29 to 0.33) suggest a relatively greater tendency for lateral expansion under stress, indicative of potential ductility.

For materials like Pr_3AlO_6 and Pr_3ScO_6 with relatively higher ductility indicated by higher Poisson's ratios, they might find application in industries requiring materials with good deformability, such as in certain forming processes or flexible structural components. On the other hand, materials like $Pr_4Al_2O_9$ and $Pr_3Sc_5O_{12}$, exhibiting higher stiffness and potentially greater strength, could be well-suited for applications demanding structural integrity and load-bearing capacity, such as in high-strength structural elements or electronic device components. The balance of these mechanical properties is crucial in tailoring materials for specific applications in fields ranging from engineering and construction to electronics and materials science, where a combination of ductility and strength is often essential.

Conclusion

The four predicted compounds (Pr_3AlO_6, $Pr_4Al_2O_9$, Pr_3ScO_6, and $Pr_3Sc_5O_{12}$) are assessed for their calculated bandgap and density of states, providing insights into their electronic properties. All of these predicted compounds exhibited significant bandgaps and high Debye temperatures, indicative of their potential utility in optoelectronic devices and photoluminescence applications. Moreover, optical absorption and emission spectra are computed for these compounds, reinforcing their suitability for photoluminescent purposes. The mechanical stability of these predictions is evaluated using the Born-Huang criterion, confirming their stability. Additionally, their high Debye temperatures further underscored their thermal stability, making them promising candidates for practical applications.

Compared to their halide counterparts, perovskite oxide derivatives are often more thermally stable and less toxic, which makes them more suitable for practical applications. The perovskite oxide derivatives have diverse design space, which allows for the incorporation of a wide range of luminescent and enables the tuning of their electronic and optical properties. In addition, the chemical space of perovskite oxide derivatives is not fully explored yet, offering a promising avenue for the development of new luminescent materials. So, this work provides insights for future experimental investigations and can lead to the development of new materials for a variety of technological applications.

Acknowledgements

This study was supported by National R &D Program through the National Research Foundation of Korea(NRF) funded by Ministry of Science and ICT (and RS-2023-00209910) and Virtual Engineering Platform Project (Grant No. P0022336), funded by the Ministry of Trade, Industry & Energy (MoTIE, South Korea). Upendra Kumar expresses sincere gratitude to Dr. Sanjay Nayak, a Senior Scientist at Silicon Austria Labs (SAL), for providing valuable motivation and inspiration to pursue work in the field of machine learning. Sobhit Singh (SS) was supported by the U.S. Department of Energy, Office of Science, Office of Fusion Energy Sciences, Quantum Information Science program under Award Number DE-SC-0020340. SS also acknowledges support from the University Research Awards at the University of Rochester.

Author contributions

Upendra Kumar and Hyeon Woo Kim conceived the idea and contributed equally to this project. Sobhit Singh provided key suggestions. Upendra Kumar wrote the manuscript and all authors read and reviewed it. Sung Beom Cho and Hyunseok Ko supervised the project.

Data availability

All data and code needed to produce the work are available from the corresponding author.

Declarations

Conflict of interest The authors declare that they have no conflicts of interest or competing interests.

Ethical approval There is no human tissue or biological material involved in this work.

Supplementary Information The online version contains supplementary material available at https://doi.org/10.1007/s10853-023-09232-6.

Appendix

Mechanical properties

The elastic tensor matrices for Pr_3AlO_6 has form:

$$C_{ij}(\text{GPa}) = \begin{bmatrix} 204.85 & 67.26 & 84.16 & 0 & 0 & 0 \\ 67.26 & 185.02 & 85.07 & 0 & 0 & 0 \\ 84.16 & 85.07 & 237.75 & 0 & 0 & 0 \\ 0 & 0 & 0 & 52.50 & 0 & 0 \\ 0 & 0 & 0 & 0 & 45.87 & 0 \\ 0 & 0 & 0 & 0 & 0 & 38.66 \end{bmatrix} \quad (5)$$

In the case of Pr_3AlO_6, which is part of the orthorhombic crystal system, the essential conditions are as follows:

1. $C_{11} > 0$
2. $C_{11} \times C_{22} > C_{12}^2$
3. $C_{11} \times C_{22} \times C_{33} + 2C_{12} \times C_{13} \times C_{23} - C_{11} \times C_{23}^2 - C_{22} \times C_{13}^2 - C_{33} \times C_{12}^2 > 0$
4. $C_{44} > 0$
5. $C_{55} > 0$
6. $C_{66} > 0$

The elastic tensor matrices for $Pr_4Al_2O_9$ has form:

$$C_{ij}(\text{GPa}) = \begin{bmatrix} 205.77 & 83.24 & 82.13 & 2.68 & 0 & 0 \\ 83.24 & 195.80 & 81.60 & -2.54 & 0 & 0 \\ 82.13 & 81.60 & 169.47 & -1.73 & 0 & 0 \\ 2.68 & -2.54 & -1.73 & 54.80 & 0 & 0 \\ 0 & 0 & 0 & 0 & 61.25 & -1.83 \\ 0 & 0 & 0 & 0 & -1.83 & 61.43 \end{bmatrix} \quad (6)$$

For $Pr_4Al_2O_9$ which belongs to the monoclinic crystal system, the necessary criteria are given as:

1. $C_{11} > 0$
2. $C_{22} > 0$
3. $C_{33} > 0$
4. $C_{44} > 0$
5. $C_{55} >$
6. $C_{66} > 0$
7. $[C_{11} + C_{22} + C_{33} + 2\times(C_{12} + C_{13} + C_{23})] > 0$
8. $C_{33}\times C_{55} - C_{35}^2 > 0$
9. $C_{44}\times C_{66} - C_{46}^2 > 0$ (x) $C_{22} + C_{33} - 2\times C_{23} > 0$
10. $C_{22}\times(C_{33}\times C_{55} - C_{35}^2) + 2\times C_{23}\times C_{25}\times C_{35} - (C_{23})^2\times C_{55} - (C_{25})^2\times C_{33} > 0$
11. $2\times[C_{15}\times C_{25}\times(C_{33}\times C_{12} - C_{13}\times C_{23}) + C_{15}\times C_{35}\times(C_{22}\times C_{13} - C_{12}\times C_{23}) + C_{25}\times C_{35}\times(C_{11}\times C_{23} - C_{12}\times C_{13})] - [C_{15}\times C_{15}\times(C_{22}\times C_{33} - C_{23}^2) + C_{25}\times C_{25}\times(C_{11}\times C_{33} - C_{13}^2) + C_{35}\times C_{35}\times(C_{11}\times C_{22} - C_{12}^2)] + C_{55}\times g > 0$ where, $g = [C_{11}\times C_{22}\times C_{33} - C_{11}\times C_{23}\times C_{23} - C_{22}\times C_{13}\times C_{13} - C_{33}\times C_{12}\times C_{12} + 2\times C_{12}\times C_{13}\times C_{23}]$.

The elastic tensor matrices for Pr_3ScO_6 has form:

$$C_{ij}(\text{GPa}) = \begin{bmatrix} 185.28 & 92.99 & 98.50 & -4.21 & -14.20 & 6.47 \\ 92.99 & 214.09 & 93.92 & -4.96 & 7.98 & -5.98 \\ 98.50 & 93.92 & 195.43 & 8.53 & -11.13 & -0.95 \\ -4.21 & -4.96 & 8.53 & 60.74 & -0.29 & -8.01 \\ -14.20 & 7.98 & -11.13 & -0.29 & 45.79 & -4.37 \\ 6.47 & -5.98 & -0.95 & -8.01 & -4.37 & 50.59 \end{bmatrix} \quad (7)$$

For Pr_3ScO_6 which belongs to the rhombohedral-2 crystal system, the necessary criteria are given as;

1. $C_{11} - C_{12} > 0$
2. $C_{13}^2 < (1/2)\times C_{33}(C_{11} + C_{12})$
3. $C_{14}^2 + C_{15}^2 < (1/2)\times C_{44}\times(C_{11}-C_{12}) = C_{44}\times C_{66}$
4. $C_{44} > 0$

The elastic tensor matrices for $Pr_3Sc_5O_{12}$ has form:

$$C_{ij}(\text{GPa}) = \begin{bmatrix} 222.24 & 82.08 & 82.08 & 0 & 0 & 0 \\ 82.081 & 222.24 & 82.081 & 0 & 0 & 0 \\ 82.081 & 82.081 & 222.24 & 0 & 0 & 0 \\ 0 & 0 & 0 & 56.54 & 0 & 0 \\ 0 & 0 & 0 & 0 & 56.54 & 0 \\ 0 & 0 & 0 & 0 & 0 & 56.54 \end{bmatrix} \quad (8)$$

For $Pr_3Sc_5O_{12}$ which belongs to the cubic crystal system, the necessary criteria are given as;

1. $C_{11} - C_{12} > 0$
2. $C_{11} + 2C_{12} > 0$
3. $C_{44} > 0$

References

[1] Fan Z, Sun K, Wang J (2015) Perovskites for photovoltaics: a combined review of organic-inorganic halide perovskites and ferroelectric oxide perovskites. J Mater Chem A 3:18809. https://doi.org/10.1039/C5TA04235F

[2] Kim J, Lee S-H, Lee JH, Hong K-H (2014) The role of intrinsic defects in methylammonium lead iodide perovskite. J Phys Chem Lett 5:1312. https://doi.org/10.1021/jz500370k

[3] Li N, Niu X, Chen Q, Zhou H (2020) Towards commercialization: the operational stability of perovskite solar cells. Chem Soc Rev 49:8235. https://doi.org/10.1039/D0CS00573H

[4] Kaminow I, Johnston W Jr (1967) Quantitative determination of sources of the electro-optic effect in linb o 3 and lita o 3. Phys Rev 160:519. https://doi.org/10.1103/PhysRev.160.519

[5] Zhu S-N, Zhu Y-Y, Ming N-B (1997) Quasi-phase-matched third-harmonic generation in a quasi-periodic optical superlattice. Science 278:843. https://doi.org/10.1126/science.278.5339.843

[6] Wojtowicz AJ, Drozdowski W, Wisniewski D, Lefaucheur J-L, Galazka Z, Gou Z, Lukasiewicz T, Kisielewski J (2006) Scintillation properties of selected oxide monocrystals activated with ce and pr. Opt Mater 28:85. https://doi.org/10.1016/j.optmat.2004.09.029

[7] Kan D, Terashima T, Kanda R, Masuno A, Tanaka K, Chu S, Kan H, Ishizumi A, Kanemitsu Y, Shimakawa Y et al (2005) Blue-light emission at room temperature from ar+-irradiated srtio3. Nat Mater 4:816. https://doi.org/10.1038/nmat1498

[8] Takashima H, Shimada K, Miura N, Katsumata T, Inaguma Y, Ueda K, Itoh M (2009) Low-driving-voltage electroluminescence in perovskite films. Adv Mater 21:3699. https://doi.org/10.1002/adma.200900524

[9] Yang S, Seidel J, Byrnes S, Shafer P, Yang C-H, Rossell M, Yu P, Chu Y-H, Scott J, Ager Iii J et al (2010) Above-bandgap voltages from ferroelectric photovoltaic devices. Nat Nanotechnol 5:143. https://doi.org/10.1038/nnano.2009.451

[10] Yasuda H, Kanemitsu Y (2008) Dynamics of nonlinear blue photoluminescence and auger recombination in srtio 3. Phys Rev B 77:193202. https://doi.org/10.1103/PhysRevB.77.193202

[11] Yamada Y, Yasuda H, Tayagaki T, Kanemitsu Y (2009) Temperature dependence of photoluminescence spectra of nondoped and electron-doped srtio 3: crossover from auger recombination to single-carrier trapping. Phys Rev Lett 102:247401. https://doi.org/10.1103/PhysRevLett.102.247401

[12] Song Z, Zhao J, Liu Q (2019) Luminescent perovskites: recent advances in theory and experiments. Inorg Chem Front 6:2969. https://doi.org/10.1039/C9QI00777F

[13] Leijtens T, Bush K, Cheacharoen R, Beal R, Bowring A, McGehee MD (2017) Towards enabling stable lead halide perovskite solar cells; interplay between structural, environmental, and thermal stability. J Mater Chem A 5:11483. https://doi.org/10.1039/C7TA00434F

[14] Jiang X, Zang Z, Zhou Y, Li H, Wei Q, Ning Z (2021) Tin halide perovskite solar cells: an emerging thin-film photovoltaic technology. Account Mater Res 2:210. https://doi.org/10.1021/accountsmr.0c00111

[15] Liu X-Y, Pilania G, Talapatra AA, Stanek CR, Uberuaga BP (2020) Band-edge engineering to eliminate radiation-induced defect states in perovskite scintillators. ACS Appl Mater Interfaces 12:46296. https://doi.org/10.1021/acsami.0c13236

[16] Kucera M, Rathaiah M, Nikl M, Beitlerova A, Lalinsky O (2022) Scintillation properties of $YAlO_3$: Ce perovskite co-doped by Mg^{2+} ions. Opt Mater 132:112779. https://doi.org/10.1016/j.optmat.2022.112779

[17] Sohrabi Anaraki H, Orekhovskaja T, Khoroshko L, Raichyonok T, Zamkovets A, Tikhomirov S (2015) Photoluminescence of terbium from strontium titanate xerogel in porous anodic alumina, in *Physics, chemistry and applications of nanostructures: proceedings of international conference nanomeeting-2015* (World Scientific, 2015) pp. 59–61, https://doi.org/10.1142/9789814696524_0014

[18] Singh R, Kaur J, Bose P, Shrivastava R, Dubey V, Parganiha Y (2017) Intense visible light emission from dysprosium (dy 3+) doped barium titanate (batio 3) phosphor and its thermoluminescence study. J Mater Sci: Mater Electron 28:13690. https://doi.org/10.1007/s10854-017-7212-z

[19] Pejchal J, Babin V, Buryi M, Laguta V, Hájek F, Páterek J, Procházková-Prouzová L, Havlák L, Czerneková V, Vaněček V et al (2022) Untangling the controversy on ce 3+ luminescence in laalo 3 crystals. Mater Adv 3:3500. https://doi.org/10.1039/D1MA01083B

[20] Sun L, Zhang C, Yan L, Gao L, Ma T (2022) Praseodymium-doped triple-cation perovskite layer for enhanced photovoltaic performance. J Solid State Chem 307:122826. https://doi.org/10.1016/j.jssc.2021.122826

[21] Vert VB, Serra JM (2010) Improvement of the electrochemical performance of $ln_{0.58}sr_{0.4}fe_{0.8}co_{0.2}o_{3-\delta}$ it-sofc cathodes by ternary lanthanide combinations (la-pr-sm). Fuel Cells 10:693. https://doi.org/10.1002/fuce.200900166

[22] Jain A, Ong SP, Hautier G, Chen W, Richards WD, Dacek S, Cholia S, Gunter D, Skinner D, Ceder G et al (2013) Commentary: The materials project: A materials genome approach to accelerating materials innovation. APL Mater 1:011002. https://doi.org/10.1063/1.4812323

[23] Xie T, Grossman JC (2018) Crystal graph convolutional neural networks for an accurate and interpretable prediction of material properties. Phys Rev Lett 120:145301. https://doi.org/10.1103/PhysRevLett.120.145301

[24] Kresse G, Furthmüller J (1996) Efficiency of ab-initio total energy calculations for metals and semiconductors using a plane-wave basis set. Comput Mater Sci 6:15. https://doi.org/10.1016/0927-0256(96)00008-0

[25] Kresse G, Furthmüller J (1996) Efficient iterative schemes for ab initio total-energy calculations using a plane-wave basis set. Phys Rev B 54:11169. https://doi.org/10.1103/PhysRevB.54.11169

[26] Perdew JP, Burke K, Ernzerhof M (1996) Generalized gradient approximation made simple. Phys Rev Lett 77:3865. https://doi.org/10.1103/PhysRevLett.77.3865

[27] Monkhorst HJ, Pack JD (1976) Special points for brillouin-zone integrations. Phys Rev B 13:5188. https://doi.org/10.1103/PhysRevB.13.5188

[28] Denault KA, Brgoch J, Gaultois MW, Mikhailovsky A, Petry R, Winkler H, DenBaars SP, Seshadri R (2014) Consequences of optimal bond valence on structural rigidity and improved luminescence properties in $Sr_xBa_{2-x}SiO_4$:Eu^{2+} orthosilicate phosphors. Chem Mater 26:2275. https://doi.org/10.1021/cm500116u

[29] Zhuo Y, Mansouri Tehrani A, Oliynyk AO, Duke AC, Brgoch J (2018) Identifying an efficient, thermally robust inorganic phosphor host via machine learning. Nat Commun 9:1. https://doi.org/10.1038/s41467-018-06625-z

[30] Ullrich B, Bhowmick M, Xi H (2017) Relation between debye temperature and energy band gap of semiconductors. AIP Adv 7:045109. https://doi.org/10.1063/1.4980142

[31] Agrawal A, Choudhary A (2016) Perspective: Materials informatics and big data: Realization of the "fourth paradigm'' of science in materials science. APL Mater 4:053208. https://doi.org/10.1063/1.4946894

[32] Villars P, Cenzual K. Pearson's crystal data®: crystal structure database for inorganic compounds (ASM International Materials Park, OH, 2007), http://www.crystalimpact.com/

[33] Hautier G, Fischer C, Ehrlacher V, Jain A, Ceder G (2011) Data mined ionic substitutions for the discovery of new compounds. Inorg Chem 50:656. https://doi.org/10.1021/ic102031h

[34] Kim HW, Han JH, Ko H, Samanta T, Lee DG, Jeon DW, Kim W, Chung Y-C, Im WB, Cho SB (2023) High-throughput screening on halide perovskite derivatives and rational design of Cs_3LuCl_6. ACS Energy Lett 8:3621. https://doi.org/10.1021/acsenergylett.3c01207

[35] Peterson GG, Brgoch J (2021) Materials discovery through machine learning formation energy. J Phys: Energy 3:022002. https://doi.org/10.1088/2515-7655/abe425

[36] Becke AD, Johnson ER (2006) A simple effective potential for exchange. J Chem Phys 124:221101. https://doi.org/10.1063/1.2213970

[37] Heyd J, Peralta JE, Scuseria GE, Martin RL (2005) Energy band gaps and lattice parameters evaluated with the heyd-scuseria-ernzerhof screened hybrid functional. J Chem Phys 123:174101. https://doi.org/10.1063/1.2085170

[38] Martin RM (2020) Electronic structure: basic theory and practical methods. Cambridge University Press, Cambridge, England

[39] Toll JS (1956) Causality and the dispersion relation: logical foundations. Phys Rev 104:1760. https://doi.org/10.1103/PhysRev.104.1760

[40] Ehrenreich H, Cohen MH (1959) Self-consistent field approach to the many-electron problem. Phys Rev 115:786. https://doi.org/10.1103/PhysRev.115.786

[41] Enamullah, Kumar V, Kumar U, Setlur GS (2014) Quantum rabi oscillations in graphene. JOSA B 31:484. https://doi.org/10.1364/JOSAB.31.000484

[42] Wang V, Xiao W, Ma D-M, Liu R-J, Yang C-M (2014) Structural, electronic, and optical properties of gaino3: A hybrid density functional study. J Appl Phys 115:043708. https://doi.org/10.1063/1.4863210

[43] Mouhat F, Coudert F-X (2014) Necessary and sufficient elastic stability conditions in various crystal systems. Phys Rev B 90:224104. https://doi.org/10.1103/PhysRevB.90.224104

[44] Singh S, Lang L, Dovale-Farelo V, Herath U, Tavadze P, Coudert F-X, Romero AH (2021) Mechelastic: a python library for analysis of mechanical and elastic properties of bulk and 2d materials. Comput Phys Commun 267:108068. https://doi.org/10.1016/j.cpc.2021.108068

[45] Kuma S, Woldemariam MM (2019) Structural, electronic, lattice dynamic, and elastic properties of $SnTiO_3$ and $PbTiO_3$ using density functional theory. Adv Condens Matter Phys 2019:1. https://doi.org/10.1155/2019/3176148

Publisher's Note Springer Nature remains neutral with regard to jurisdictional claims in published maps and institutional affiliations.

Springer Nature or its licensor (e.g. a society or other partner) holds exclusive rights to this article under a publishing agreement with the author(s) or other rightsholder(s); author self-archiving of the accepted manuscript version of this article is solely governed by the terms of such publishing agreement and applicable law.